UCLA
UCLA Previously Published Works

Title

Strategic Placement of Accelerometers for Structural Health Monitoring of a Complex Unreinforced Stone Masonry Hindu Mandir

Permalink

https://escholarship.org/uc/item/1sv3k1b2

Journal

International Journal of Architectural Heritage, ahead-of-print(ahead-of-print)

ISSN

1558-3058

Authors

Abu Shehab, Hala

Kishida, Tadahiro

Bouchaala, Fateh

et al.

Publication Date

2024

DOI

10.1080/15583058.2024.2323031

Copyright Information

Peer reviewed

Strategic Placement of Accelerometers for Structural Health Monitoring of a Complex Unreinforced Stone Masonry Hindu Mandir

Hala Abu Shehab, Tadahiro Kishida, Fateh Bouchaala, Snehalkumar Patel, Elia Voyagaki, Tae-Yeon Kim & Maryam Rashed Al Shehhi

Published online: 04 Mar 2024.

Submit your article to this journal ☑

View related articles ☑

View Crossmark data ☑

Taylor & Francis
Taylor & Francis Group

RESEARCH ARTICLE

OPEN ACCESS | Check for updates

Strategic Placement of Accelerometers for Structural Health Monitoring of a Complex Unreinforced Stone Masonry Hindu Mandir

Hala Abu Shehab[a], Tadahiro Kishida[a,b], Fateh Bouchaala[c], Snehalkumar Patel[d], Elia Voyagaki[a,e], Tae-Yeon Kim[a], and Maryam Rashed Al Shehhi[a]

[a]Department of Civil and Environmental Engineering, Khalifa University of Science and Technology, Abu Dhabi, UAE; [b]Department of Civil and Environmental Engineering, University of California, Los Angeles, USA; [c]Department of Earth Sciences, Khalifa University of Science and Technology, Abu Dhab, UAE; [d]Satt Engineering Ltd, Edmonton, Canada; [e]School of Civil, Aerospace and Design Engineering, University of Bristol, Bristol, UK

ABSTRACT

The BAPS Hindu Mandir, recently constructed in Abu Dhabi, UAE, is a complex unreinforced stone masonry structure built from thousands of sculpted sandstone and marble pieces employing ancient Indian techniques called Shilp Shastra. The entire structure is substantially large with a footprint size of 5,100 m^2 and unique so that it is not covered by modern seismic design standards. Its performance was verified by conducting dynamic field tests presented herein. The most vulnerable substructure was identified based on both engineering judgement and modal analysis of the entire structure employing a detailed 3D finite element model, which was validated via the field experiments. A "local" model was developed for the identified vulnerable substructure which significantly reduced model complexity and allowed to overcome computational limitations. Based on the response of the local model, the relative importance of the sensor locations was determined via a Displacement Index method in addition to a reduction of the total variance of spectral accelerations using conditional probability theory. Through this approach, a methodology for selecting the optimal sensor placement with application on the complex unreinforced stone masonry Hindu Mandir is proposed.

1. Introduction

Structural health monitoring (SHM) is a key process for obtaining crucial and comprehensive information from large-scale civil structures by installing sensors (Housner et al. 1997). SHM is used to identify the structural systems, calibrate physics-based models and detect damage at early stages to maintain life safety and mitigate economic losses (Aktan and Brownjohn 2013; Farrar and Worden 2007; Ng 2014; Todorovska and Trifunac 2007). SHM consists of several components such as sensor placement, data acquisition and transmission, structural health evaluation and database management/decision making systems (Basto, Pelà, and Chacón 2017; Cawley 2018; Pregnolato et al. 2022; Yi, Li, and Gu 2011b). This is especially important for structures designed and constructed using ancient techniques, such as the stone temple at hand, not covered by modern design standards (Cigada et al. 2017). Masonry heritage structures are especially valuable from a cultural viewpoint and particularly important to preserve, hence they have attracted strong research attention regarding their seismic performance (Casapulla, Argiento, and

Maione 2018; D'Ayala and Lagomarsino 2015; Lagomarsino and Cattari 2015; Pardalopoulos and Pantazopoulou 2017; Torelli et al. 2020). It is also recognized that these structures have unique failure modes under high frequency vibrations (e.g. 5–10 Hz) due to relative displacements between the stones as well as low-frequency excitations at resonance frequencies (Meyer et al. 2007; Silvestri et al. 2021). The BAPS Hindu Mandir in Abu Dhabi is a highly complex unreinforced stone masonry heritage structure that provides an ideal candidate for applying SHM methodologies to evaluate its performance over short and long periods.

Accelerometers are often installed to monitor changes in the natural frequencies of a structure due to their sensitivity to damage (García-Macías and Ubertini 2022; Sivori, Cattari, and Lepidi 2022; Todorovska and Trifunac 2007) and provide a relatively low cost solution for SHM (Barsocchi et al. 2021; Kim et al. 2007; Herráiz et al. 2016). The simplest approach involves two accelerometers, at foundation and roof levels (Todorovska and Trifunac 2007), although accuracy naturally increases for

denser networks. The evolution of the mode shapes in successive measurements is analyzed to detect damage (Carne and Dohrmann 1994; Pandey, Biswas, and Samman 1991; Rytter 1993). For instance, Modal Assurance Criterion is an index for evaluating the correlation of the vibration periods between two successive events (Allemang 2003; Li, Der Kiureghian, and Au 2018; Pastor, Binda, and Harčarik 2012; Wiercigroch 2018) and is used as a damage indicator (Altunışık, Okur, and Kahya 2017; Jassim et al. 2013). Vibration energy against external excitation can also be analyzed to detect structural damage (Muin and Mosalam 2017; Sun and Chang 2004), where the difference in the distributed energy pattern in successive measurements is a damage indicator. Wave travel time has been utilized to detect damages between the sensors for buildings (Behnia et al. 2014; García-Macías and Ubertini 2022; Lacanna et al. 2019; Ludeno et al. 2020) and earth structures (Kishida et al. 2020). Through these methods, global and local structural damage can be detected by monitoring acceleration signals. Application examples on cultural heritage structures are available (Ceravolo et al. 2016).

SHM requires a reliable, and calibrated on observed data, structural model for conducting numerical analyses that provides understanding of how the structure performs under induced displacements and strains (Çatbaş, Kijewski-Correa, and Aktan 2013). For historical structures in particular, past studies emphasize the importance of field monitoring because the observed response does not generally match the calculated one from uncalibrated numerical models (Castellazzi et al. 2017). The mismatch can be explained in view of the complexity of those structures including the construction techniques and materials that differ from the contemporary ones, which makes it difficult to simulate numerically (Castellazzi et al. 2017; Cigada et al. 2017). Therefore, the calibration of the numerical models are important with the observed signals using evolutional and updating approaches such as genetic algorithm and Bayesian statistics (Bianconi et al. 2020; Monchetti et al. 2023; Salachoris et al. 2023; Standoli et al. 2021). Especially for large/extended structures, it is important to understand the expected damage and failure modes in order to optimize sensor placement and overcome budget restrictions as well as computational limitations. To this end, substructure models can be developed for the vulnerable parts of the structure (Koh, Hong, and Liaw 2003; Oreta and Tanabe 1993). The advantage in using a substructure model is that the analyses and computational time can be significantly simplified/reduced. The main disadvantage is that in order to select the local (substructure) model one needs to identify the vulnerable locations for selected loading conditions.

Past studies have developed surrogate models to mimic the structural response while simplifying the FE analyses via statistical algorithms (Yang et al. 2022). This is a different approach to the one presented herein which involves selecting critical substructures, based on engineering judgement.

Accelerometers are often installed at locations where large displacements are expected. Moussas and Pnevmatikos (2019) suggested using a Displacement Index (DI) for simple structures, which is an inner product of nodal displacements and associated mass vectors. For each node, the total index is evaluated from the sum of all significant modes to cover 90% of the participating mass, following Eurocode 8 (2004). However, the main disadvantage of this approach is that the correlation between the sensor locations was not considered. Reviews of optimal sensor placement studies have been published recently (e.g. Hassani and Dackermann 2023; Tan and Zhang 2020). The OSP were often determined to effectively capture the different modal shapes (e.g. Chang and Pakzad 2014; Gomes et al. 2019; Yao, Sethares, and Kammer 1993). For relatively simple structures, sequential sensor placement (SSP) algorithms are often employed that search, for example, for the maximum reduction of off-diagonal MAC elements (Yi, Li, and Gu 2011a). For complex systems, sufficient optimization algorithms are required with mathematical transition rules, including genetic algorithm (e.g. Abdullah, Richardson, and Hanif 2001; Guo et al. 2004; Yi, Li, and Gu 2011b), simulated annealing algorithm (Chiu and Lin 2004; He and Hwang 2006), and particle swarm optimization algorithm (Li et al. 2015). Uncertainties in model parameters can also be considered using Bayesian optimization (Argyris, Papadimitriou, and Panetsos 2017). Similar methodologies were adopted in prior studies (Abdullah, Richardson, and Hanif 2001; Chang and Pakzad 2014; Gomes et al. 2019; Vuran, Akan, and Akyildiz 2004).

This study discusses the optimal sensor placement on the BAPS Hindu Mandir in Abu Dhabi. To this end, a detailed finite element (FE) model has been developed for the entire structure. Based on preliminary time series analyses, Main Shikhar was considered to be the most vulnerable substructure against seismic excitation. Field monitoring was conducted at the construction site to validate the developed FE model. Seismometers were installed at the free-field and different structural elevations. Impact loadings were provided by dropping a concrete mass at an adjacent site. The vibration periods were identified by processing the recorded signals. The measured periods were compared with the results by the FE simulations for model validation. To reduce the

structural complexity, a local model of the vulnerable substructure was developed considering an average stiffness matrix with linear-elastic springs at the structural boundaries, based on lateral load analyses. Modal response analyses were conducted for the developed local model. A total of 13 locations were selected for potential sensor placement based on the DI methodology. Time series analyses of the local model were conducted to extract pseudo-spectral accelerations (PSAs) at different FE nodes. The importance of each location was determined based on the reduction of the total variance of the PSA conditioned on the selected location instead of using the descending order in DI. The details of these processes, to strategically select accelerometer locations for the effective SHM of a complex unreinforced stone masonry Hindu Mandir in Abu Dhabi, are described in the following sections.
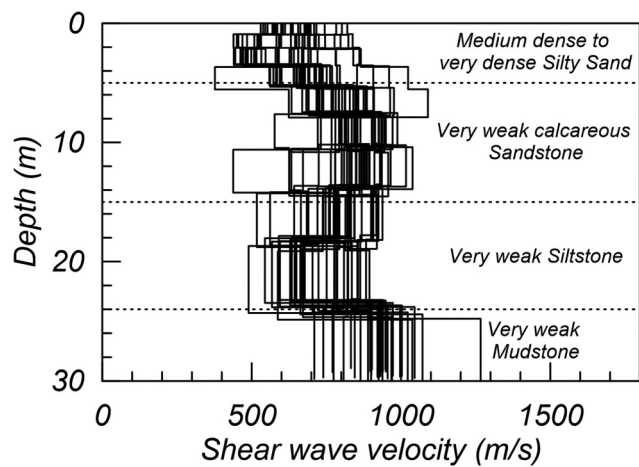
2. The BAPS Hindu mandir in Abu Dhabi

2.1. Construction site

An unreinforced stone masonry Hindu Mandir is under construction in the north of the city of Abu Dhabi. The site is located in Abu Mureikhah. The site has an area of 50,000 m^2 out of which the main structure occupies 5,100 m^2. The groundwater level was detected 6 m from the ground free surface. Table 1 shows the soil profile obtained by a series of standard penetration tests. Subsurface sand deposits have a thickness of 5 m underlain by a 10-m thick sandstone layer. Siltstone, mudstone, and gypsum layers exist beneath the sandstone. The unconfined compression strength of the retrieved samples was 3 MPa for the sandstone and increased to 6–15 MPa at a depth of 30 m. Figure 1 provides shear wave profiles measured by Multi-Channel Analysis for Surface Waves (MASW) (Park, Miller, and Xia 1999). The shear wave velocity was approximately 500–700 m/s at the ground surface and gradually increases to 800 m/s at a depth of 30 m. The averaged shear wave velocity within the top 30 m is 765 m/s, corresponding to site class B, following the International Building Code (ICC 2018). The

Figure 1. Subsurface shear-wave velocity profiles at the construction site obtained by MASW.

concrete raft foundation supporting the structure was constructed on the sandstone layer after removing the top sand deposits.

2.2. Description of the structure

Figure 2 shows the entire Hindu temple image. The plan and cross-section views are provided in Figure 3a and b, respectively. The lower section is made of granite over which distinctive pink sandstone from Rajasthan is added. The temple consists of the Ground, Jagati, First, and Terrace floors, in addition to the massive Dome, Shikhar and Ghumat Towers. Figure 4 shows the plan views at different floor levels. The main Shikhar tower is connected to the rest of the structure at the Jagati, First and Terrace floor levels, where the connecting locations are illustrated in Figure 4. This is a typical Hindu Mandir structure found in various historical monuments such as Kashi Vishwanath in India and Angkor Wat in Cambodia. Figure 5 shows the sculpted stone pieces of Hindu Mandir, (a) exterior sandstone wall and (b) structural marble column on first floor, respectively. These pieces are interlocked without using connecting mortar.

3. Structural modeling

3.1. Methodology

Figure 6 presents the methodology to develop a local structural model of the large unreinforced stone masonry for optimal sensor placement. A mathematical framework established in past studies (Koh, Hong, and Liaw 2003; Oreta and Tanabe 1993) has been adopted. A FE model was developed

Table 1. Lithology of multi-layered subsurface based on data interpretation of 13 boreholes.

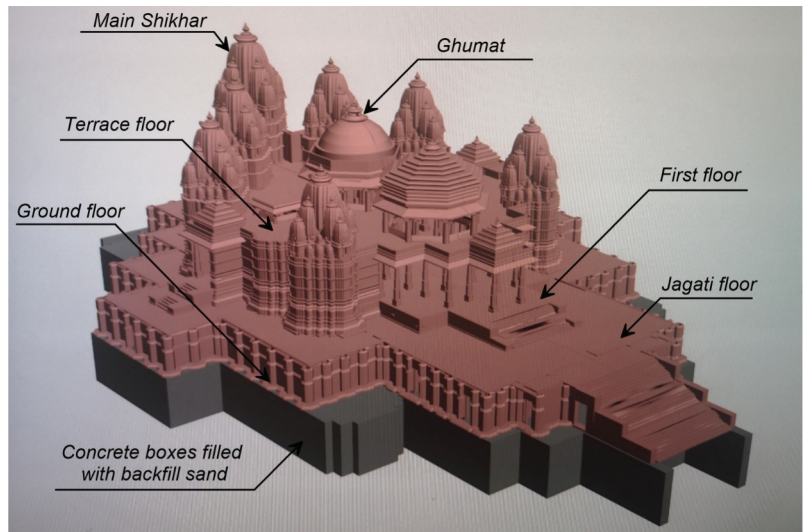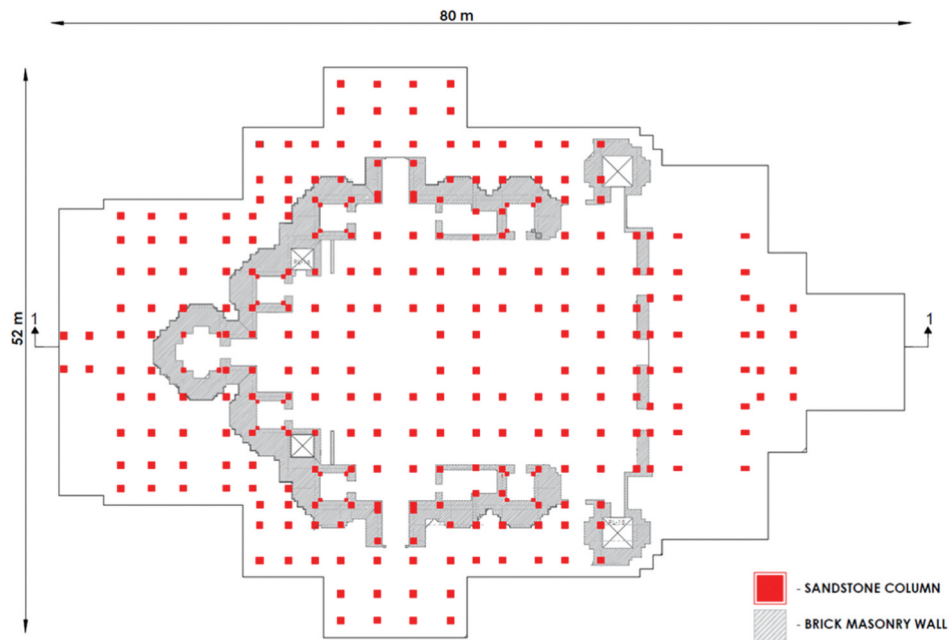| Depth (m)	General lithology
0–5	Medium dense to very dense Silty Sand
5–15	Very weak calcareous Sandstone
15–24	Very weak Siltstone
24–31	Very weak Mudstone
31–37	Very weak to weak Gypsum

Figure 2. An image of the BAPS Hindu mandir in Abu Dhabi.

(a) Plan view at ground floor
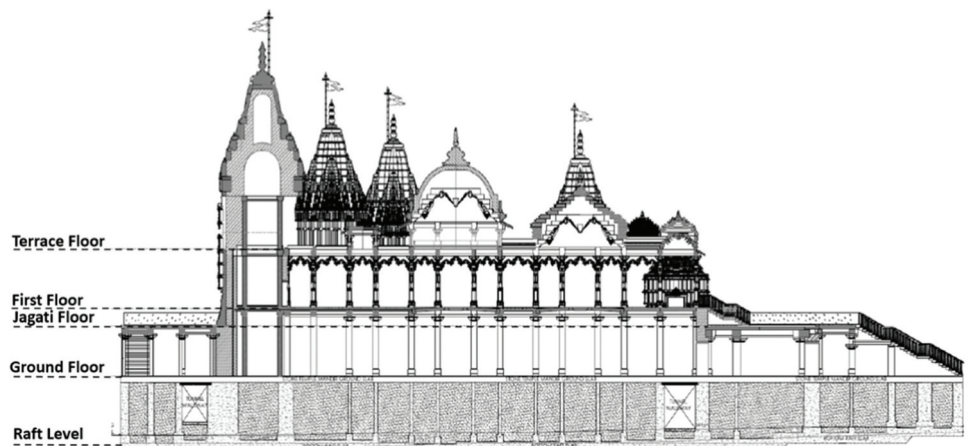
(b) Section 1-1 through Main Shikhar Tower

Figure 3. Drawings of BAPS Hindu mandir in Abu Dhabi (a) plan view at ground floor and (b) cross-section view through main Shikhar.
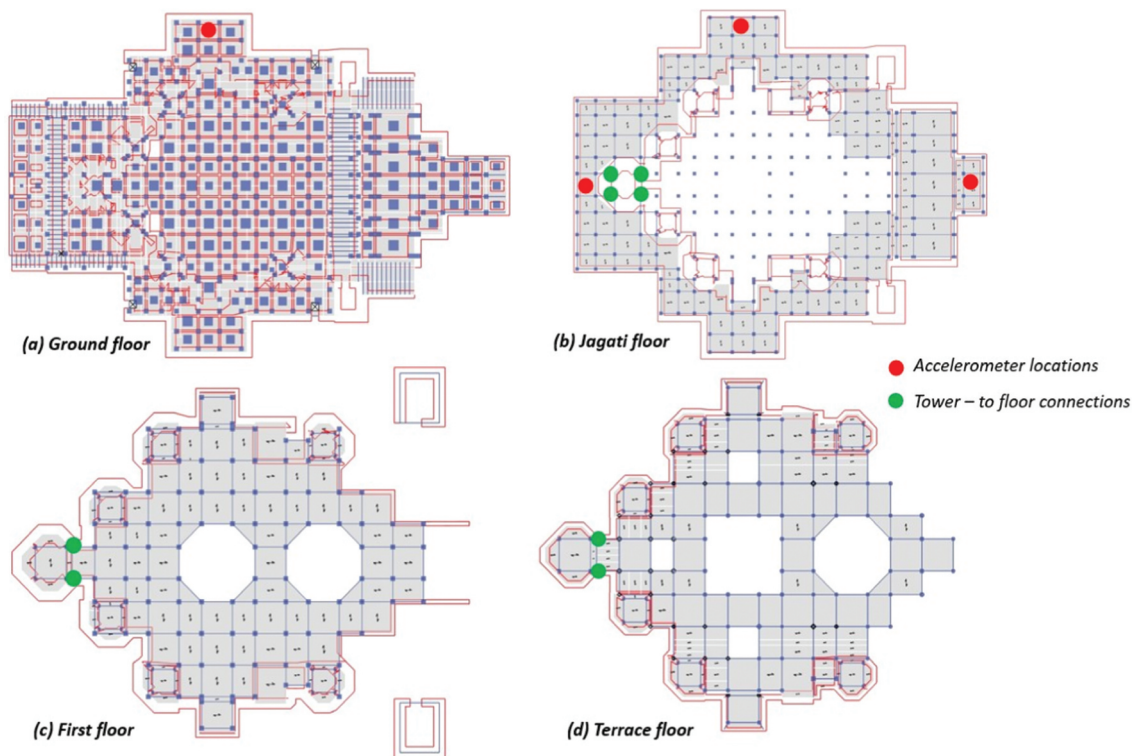
Figure 4. Plan view of: (a) Ground; (b) Jagati; (c) first and (d) terrace floors. Locations of the four field testing seismometers are indicated with red dots. Connection points of the main Shikhar to the floor levels are shown by green dots.
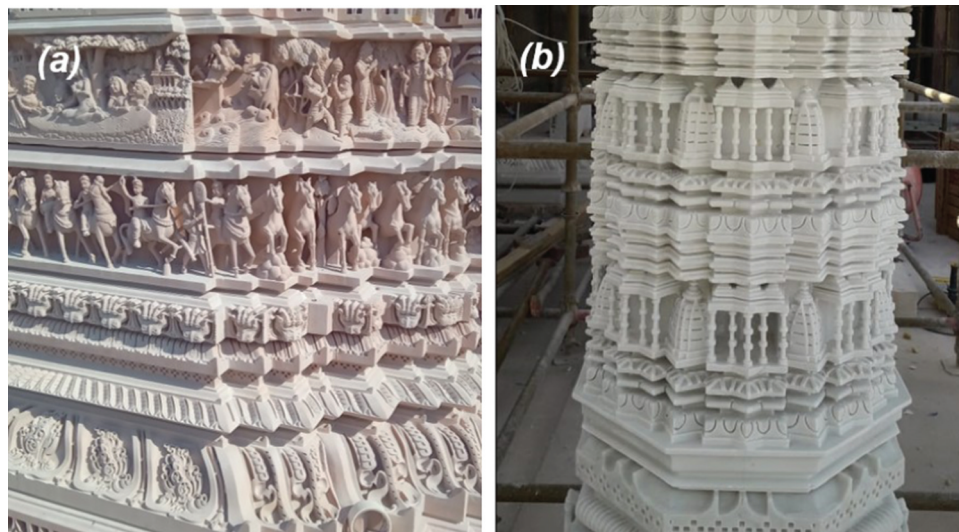
Figure 5. Example pictures of sculpted stone pieces of Hindu mandir, (a) exterior sandstone wall on the first floor, (b) structural marble column on the first floor.

for the entire structure (Figure 6a). The most vulnerable substructure against seismic excitation is identified by time series analysis (Figure 6b). An interface connecting the substructure to the rest of structure was developed using an average stiffness matrix of linear-elastic springs based on lateral load analyses (Tena-Colunga 1992) (Figure 6c). A local model was developed for the substructure (Figure 6d). The FE model was calibrated using measured responses from field monitoring during
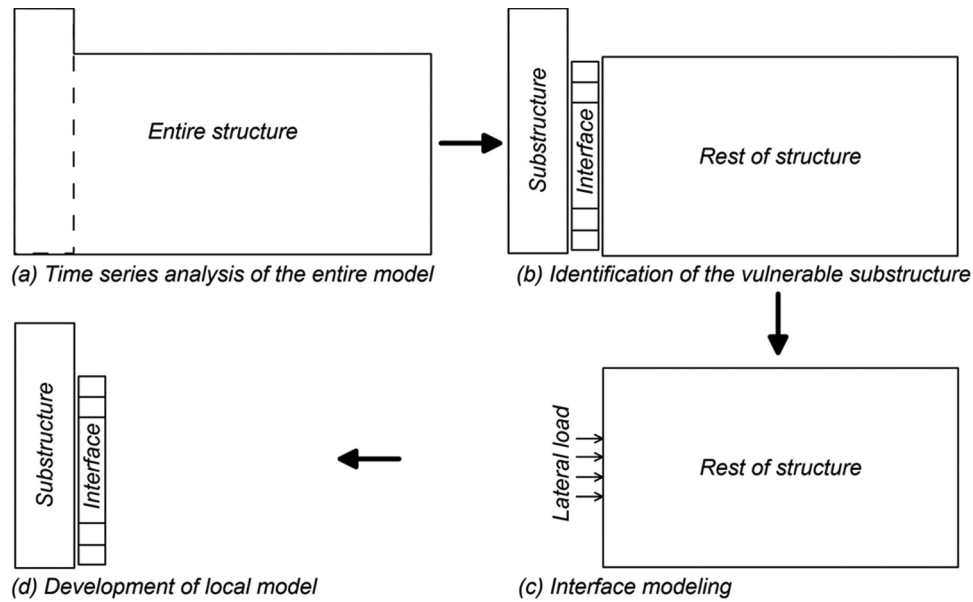
Figure 6. Methodology for splitting the FE model to develop a local model of the vulnerable substructure.

construction stages. The "local" FE model significantly reduced computational complexity and was used for the determination of optimal sensor placement.

3.2. "Global" FE Model of the entire structure

Figure 7 shows the 3D-FEM of the structure developed in ETABS (CSI 2018). The major structural elements are slabs, beams, columns, walls, and foundations. The total number of elements and nodes are 1,433 and 4,619, respectively. Table 2 summarizes the material properties which were obtained by conducting laboratory experiments following the Indian Standard Code IS 1905 (1987). The foundation system includes compacted sand within the concrete box rested on raft. Its weight is approximate 25,000 *tons* and heavier than the upper structure by 40%. Carrara marble and clay bricks are used for the upper structure. The slabs are modeled as rigid diaphragms. Actual slab thicknesses were assigned to accurately model their masses. Beams and columns embedded within the wall area were linear elements of square and rectangular shapes. Wall thicknesses were applied as an equivalent thickness based on the weighted average of the wall area. The Mandir's foundation consists of concrete boxes filled with compacted backfill sand. The concrete boxes were modelled by shell elements. The backfill sand was modelled by sand columns with truss elements, where the sand columns were placed

without any separation distance between each other. The sand columns were assigned the material properties reported in Table 2.

Both static and dynamic loading were considered. Static conditions encompass the self-weight of the structure, as well as live loads. Seismic loads were determined by the Abu Dhabi International Building Code (ADIBC) (DMA 2013). The peak ground acceleration was taken equal to .173g with an annual exceedance probability of 10% in 50 years. Spectral acceleration at a short (S_S) and 1-second period (S_1) were .65 and .2g, respectively, for site class B. Preliminary time series analyses were conducted using the entire model. The Main Shikhar demonstrated a longest period of .3 s and the largest displacements within the entire structure. This observation indicates that the Main Shikhar is potentially vulnerable to seismic loads. Therefore, the local model was developed for the Main Shikhar as major damage is expected in this particular substructure.

3.3. "Local" FE Model of the main shihkar

Figure 8 illustrates the local model of the Main Shikhar that has been detached from the global model (Figure 7). Green dots show the connections to the rest of the structure. Two types of boundary conditions were assigned: (1) a rigid boundary at the Main Shikhar's base on the massive foundation and (2) a flexible boundary between Main Shikhar and the rest of the structure. For the flexible boundary conditions, the springs were placed at the points where the
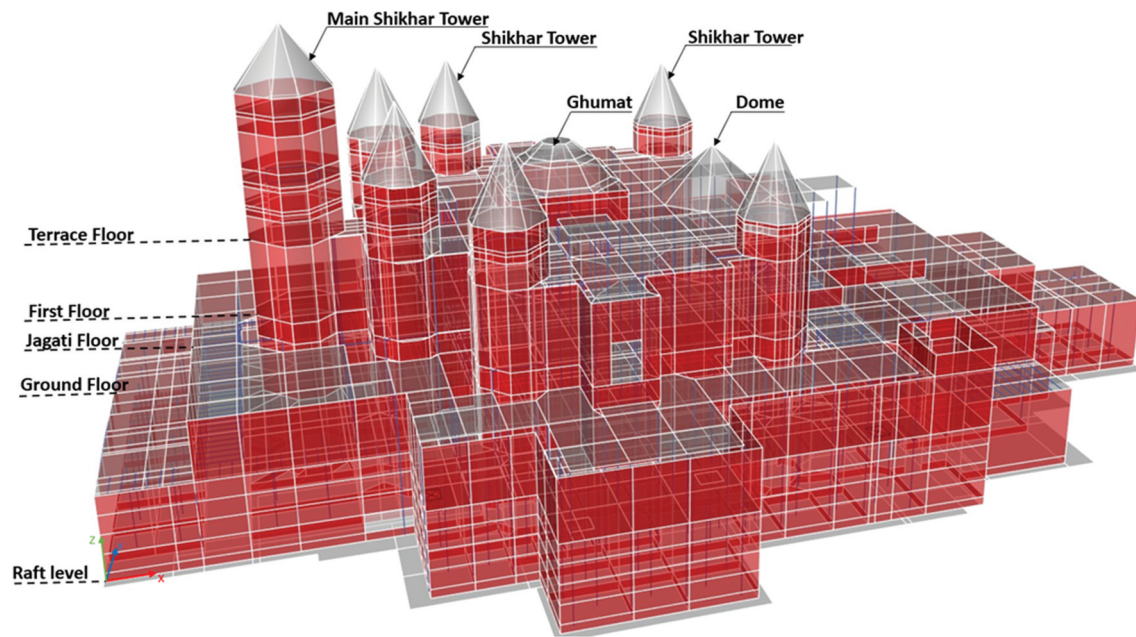
Figure 7. An entire structure model of a stone unreinforced Hindu mandir.

Table 2. Material specifications.

Property	Concrete		Sandstone	Carrara marble	Clay brick	Sand fill
Unit weight (kN/m^3)	22–25	22–25	22.75	27.11	18	18
Poisson ratio	0.20	0.20	0.28	0.28	0.20	0.20
Modulus of elasticity (MPa)	33,500	28,200	63,400	60,600	413	80.0
Compression strength (MPa)	60.0	45.0	69.3	88.9	8.89	-
Water absorption (%)	5.00	5.00	2.42	-	13.9	-
Average flexural strength (MPa)	1.780	1.510	24.1	22.7	-	-
Average shear strength (MPa)	-	-	6.00	5.31	-	-
Thermal conductivity (W/mk)	1.680	1.680	-	1.810	.00840	-
Coefficient of thermal expansion (/c)	9.90E–6	9.90E–6	1.170E–5	6.30E–5	1.170E–5	9.90E–6
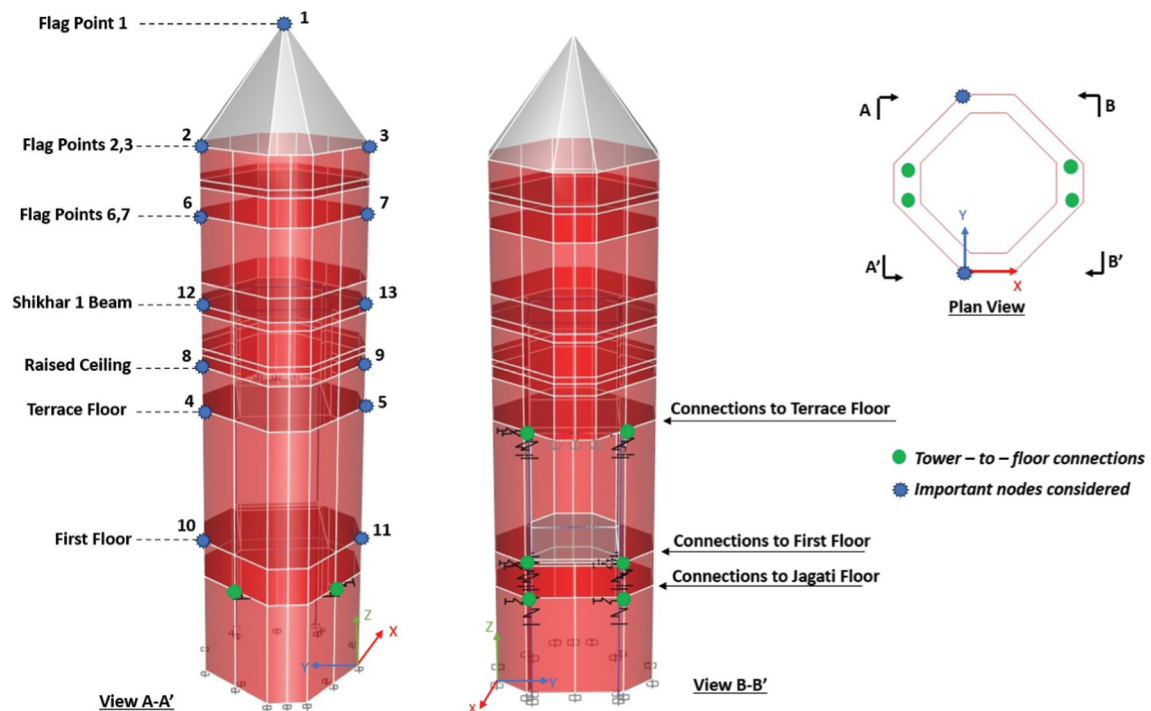
Figure 8. A local structure model of main Shikhar.
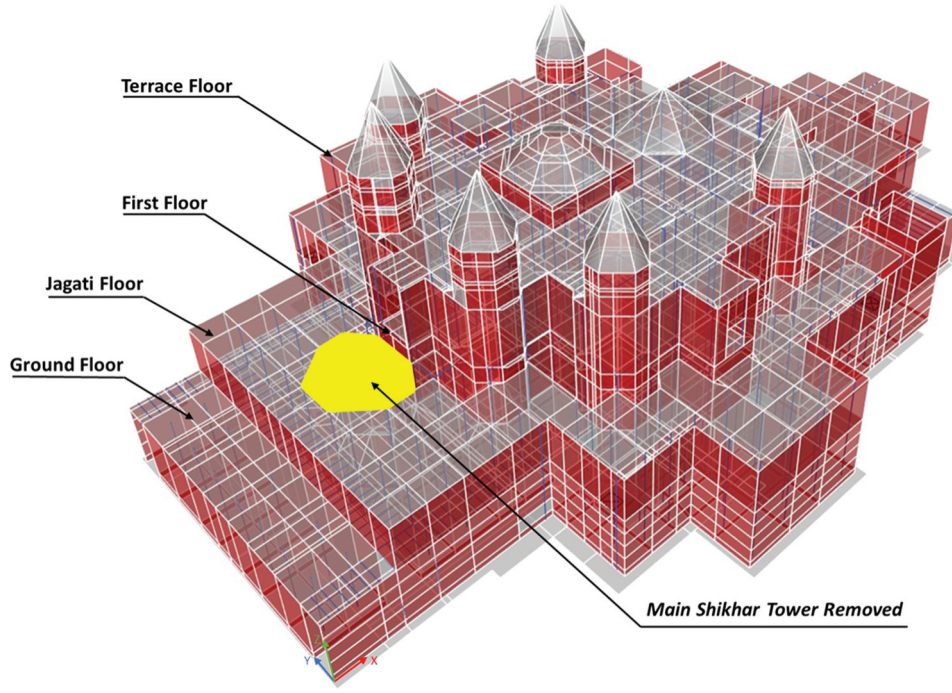
Figure 9. Global model without main Shikhar.

Main Shikhar is connected with the rest of the structure (green dots in Figure 4). Figure 9 shows the rest-of-structure model where Main Shikhar is detached from the global model. The point loads of P_1, P_2 and P_3 were applied to the Jagati, First, and Terrace floors independently at the middle of connecting points with the Main Shikhar. Displacements (U) at each level were obtained for each applied load. For instance, the displacements at the Jagati, First, and Terrace floors due to force P_1 were denoted as U_{11}, U_{21} and U_{31}. This process produces a 3×3 stiffness matrix as follows (Tena-Colunga 1992).

$$\begin{bmatrix} P_1 & 0 & 0 \\ 0 & P_2 & 0 \\ 0 & 0 & P_3 \end{bmatrix} = \begin{bmatrix} K_{11} & K_{12} & K_{13} \\ K_{21} & K_{22} & K_{23} \\ K_{31} & K_{32} & K_{33} \end{bmatrix} = \begin{bmatrix} U_{11} & U_{12} & U_{13} \\ U_{21} & U_{22} & U_{23} \\ U_{31} & U_{32} & U_{33} \end{bmatrix} \quad (1)$$

By solving the above equation, the interface stiffness terms K_{ij} were obtained for two horizontal directions in Table 3. The spring stiffnesses for each level were calculated from the translational values in Table 3 divided with the number of springs at that level. A similar methodology has been applied in the past to model flexible diaphragms in masonry structures (Tena-Colunga 1992).

The equation of motion of the structural system can be expressed as follows (Koh, Hong, and Liaw 2003; Oreta and Tanabe 1993):

Table 3. Stiffness matrices K_X & K_Y for X and Y directions for the Jagati, first, and terrace floors.

K_X (kN/m)		
100,000,000	−72,000,000	510,000
−72,000,000	67,000,000	−1,990,000
510,000	−1,990,000	1,400,000

K_Y (kN/m)		
50,000,000	−34,000,000	760,000
−34,000,000	35,000,000	−3,500,000
760,000	−3,500,000	2,600,000

$$\begin{bmatrix} M_{rr} & M_{ri} & 0 \\ M_{ir} & M_{ii} & M_{is} \\ 0 & M_{si} & M_{ss} \end{bmatrix} \begin{bmatrix} x_r \\ x_i \\ x_s \end{bmatrix} + \begin{bmatrix} C_{rr} & C_{ri} & 0 \\ C_{ir} & C_{ii} & C_{is} \\ 0 & C_{si} & C_{ss} \end{bmatrix} \begin{bmatrix} \dot{x}_r \\ \dot{x}_i \\ \dot{x}_s \end{bmatrix}$$
$$+ \begin{bmatrix} K_{rr} & K_{ri} & 0 \\ K_{ir} & K_{ii} & K_{is} \\ 0 & K_{si} & K_{ss} \end{bmatrix} \begin{bmatrix} x_r \\ x_i \\ x_s \end{bmatrix} = \begin{bmatrix} L_r F_r \\ L_i F_i \\ L_s F_s \end{bmatrix}$$
$$(2)$$

where M, C, and K are the mass, damping and stiffness matrixes, respectively, while F and L are the external forces and mapping matrix, respectively. Subscripts r, i, s denote the "rest of structure", "interface" and "substructure" in Figure 6. From Equation (2) the substructure response can be obtained by assuming that the structures are connected with rigid diaphragm (i.e. $x_s = x_i = x_r$).

$$M_{ss}\ddot{x}_s + C_{ss}\dot{x}_s + K_{ss}x_s + M_{rr}\ddot{x} + C_{rr}\dot{x}_r + K_{rr}x_r$$
$$= L_sF_s + L_rF_r - L_iF_i + M_{ii}\ddot{x} + C_{ii}\dot{x}_i + K_{ii}x_i \quad (3)$$

The interface represents the connection of the substructure and the rest of structure; therefore, its action implicitly assumes no mass and no external force from outside of the system ($M_{ii} = L_iF_i = 0$). The stiffness and viscosity of the interface are similarly considered to be negligible compared to the rest of structure (i.e. $K_{ii} \ll K_{rr}$, $C_{ii} \ll C_{rr}$). The rest of structure is approximated by pseudo-static behavior (i.e. $\ddot{x} = \dot{x}_r = L_rF_r = 0$). Given these assumptions, the following equation is obtained:

$$M_{ss}\ddot{x}_s + C_{ss}\dot{x}_s + K_{ss}x_s = L_sF_s - K_{rr}x_s. \quad (4)$$

These assumptions are reasonable on the basis of the structural system (Koh, Hong, and Liaw 2003). The local model of the Main Shikhar was developed using the spring stiffness by Equation (1) at the boundary with the rest of the structure, to conduct dynamic analyses.

3.4. Vibration modes of the mandir

The linear modal analysis was conducted in ETABS. The first and second mode shapes for the global and local models, were translational along the Y and X directions, respectively, as presented in Figures 10 and 11. The fundamental periods of the global and local models were .33 s and .26 s, respectively. For the second mode shape, the natural periods were .30 s and .23 s for the global and local models, respectively. For the first mode, the largest nodal displacements were observed at the top of Main Shikhar for both models (Figures 10a and b),
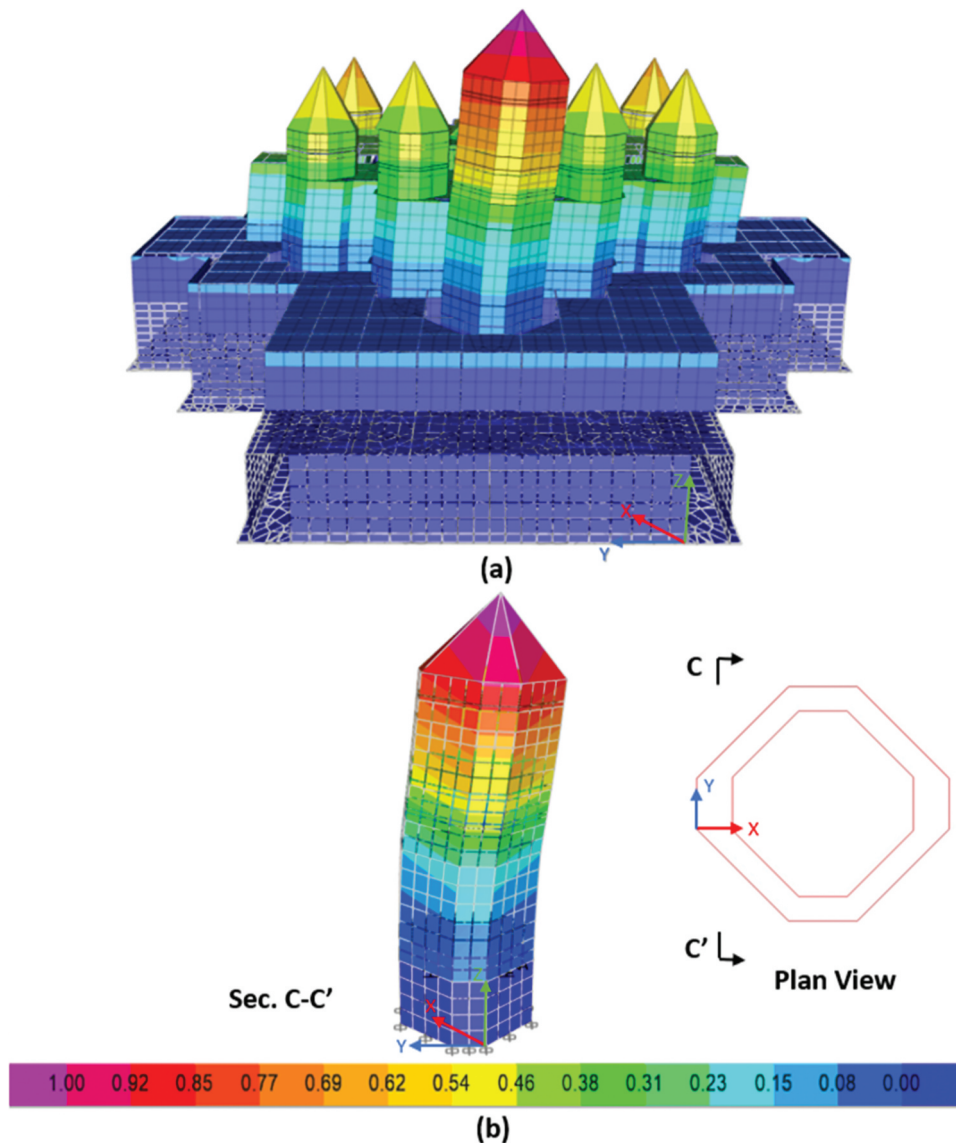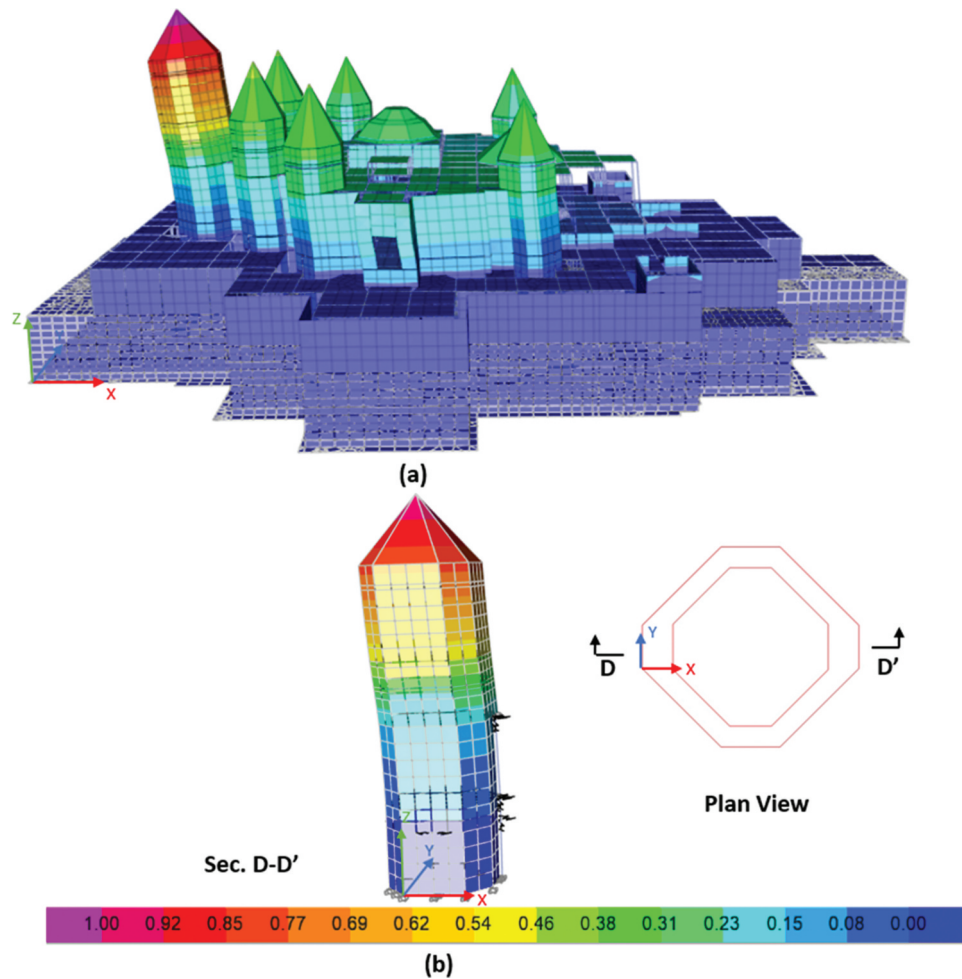

Figure 10. The first mode shape of (a) the global model and (b) the local model.

Figure 11. (a) the second mode shape of the global model (b) the second mode shape of the local model.

while the displacement becomes negligible below the connections at the first floor level. Similar observations can be made in Figures 11a and b. As the eigenmodes for global and local models are sufficiently similar, it can therefore be concluded that the dynamic behavior of the Main Shikhar is sufficiently separated by the local model.

3.5. Model validation by field observations

Four seismometers were installed on the structure upon completion of the first-floor level on April 30, 2022. One seismometer was placed at ground level and three were installed at the corners of the first-floor level (red dots in Figure 4). The noises were reduced by covering the sensors with soil or bricks (Figure 12). This process enhances its stability by preventing resonance and rocking from wind due to poor coupling with the soil, by which sources of noise unrelated with field testing are eliminated. The structural vibrations were induced using impact loads, by dropping a 2.5-ton concrete weight at a distance of 50 m from the structure (Figure 13). In total, nine measurements were recorded by dropping the weight at different locations. Table 4 provides the technical specification of the installed seismometers, while Figure 14 shows their amplitude and phase response with a sampling frequency of 100 Hz. Instrument response is flat from .02 to 10 Hz (Nanometrics inc 2015) (Figure 14a). As this study applied instrument correction, the measured signals are reliable up to a frequency of 40 Hz with the applied anti-alias filter. Signals were stored in MiniSEED formats.

A Python routine was employed for the data processing after converting their format from MiniSEED to stream objects using ObsPy (Krischer et al. 2015; Megies et al. 2011). Since the seismometers measured continuous signals, the associated signals due to impact loads were extracted from the four recordings by selecting the time windows of the impact. Figure 15 shows an example of a velocity time series recorded during impact at
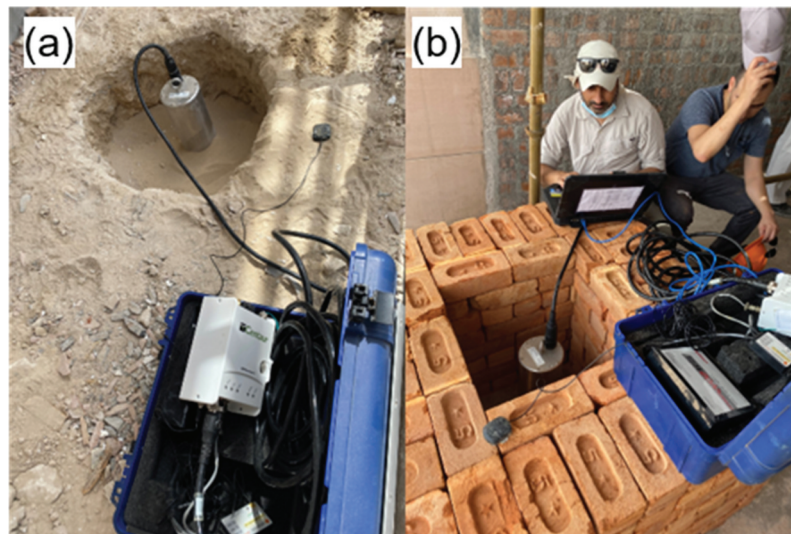
Figure 12. Installed seismometers at (a) ground and (b) first floor levels.

Figure 13. Impact load generation by a concrete mass.

Table 4. Seismometer and digitizer specifications (Nanometrics inc. 2015).

Seismometer Name	Trillium Posthole Seismometer
Seismic Acquisition System	Centaur digital recorder
Digitizer Type	24-bit ADC per channel
Digital Filter	140 dB attenuation at output Nyquist
Filter Type	Linear phase
Resolution	24-bits per channel
Recording Format	MiniSEED
Sample Rates	100 Samples Per Second (Hz)
Sensitivity	3.02E8 count/(m/s)
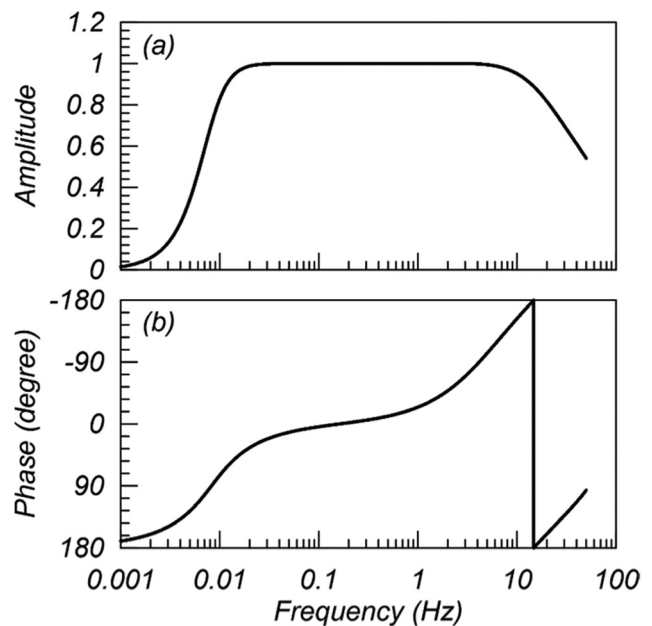
Figure 14. Instrument responses of the installed seismometers (a) amplitude response and (b) phase response.

ground and first-floor levels. It shows a clear peak with an approximate duration of .5 s. The amplitude at the first-floor level is roughly three times higher than that the ground level. Velocity time series were converted to accelerations by taking the derivative in the frequency domain. Since the signal shows the baseline drift in displacement time series, the Butterworth high-pass filter was applied at .01 Hz (Chamberlain et al. 2018).

Figure 16 shows the flowchart of computing the Transfer Functions (TF). Fourier Amplitude Spectra (FAS) were computed from the acceleration time series. The FAS was smoothed using the Konno-Ohmachi
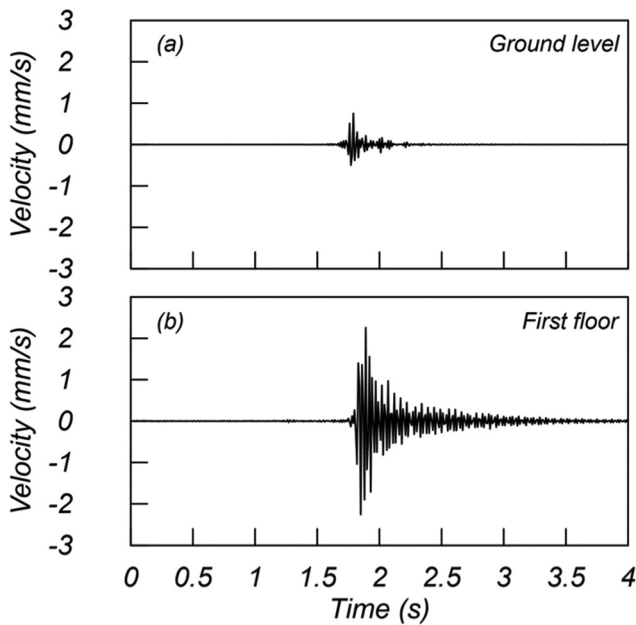
Figure 15. Example of a recorded velocity time series in the Y direction generated by impact loads (a) ground-floor level and (b) first-floor level.

Figure 16. Flowchart of adopted approach for computing the transfer functions.

window which does not distort the amplification factor and the associated resonance frequencies (Konno and Ohmachi 1998). A smoothing parameter of $b = 30$ was used based on visual inspection. The selected b value is consistent with past studies for computing the site resonant periods (Ktenidou et al. 2016; Woolery, Street, and Hart 2009). TFs were calculated by dividing the FAS on the first floor by the ones on the ground level, which is conventional approach in the past studies (e.g. Borcherdt and Gibbs 1976; LeBrun, Hatzfeld, and Bard 2001). The averaged TF for each direction was calculated by stacking nine TFs from impact loads. The resonance frequencies correspond to the peak values of the TFs (Park and Kishida 2019; Zhu, Cotton, and Pilz 2020). Figure 17 depicts the FAS at ground and first-floor levels and TF in X and Y directions. Figure 17c suggests that the FAS gradually increases as frequency decreases at ground level (red line) when the frequency is less than 2.5 Hz. This observation indicates that environmental noise dominates below 2.5 Hz. The observed TF in Figure 17d exhibits a magnitude of approximately 1 in the frequency range from 2.5 to 6 Hz, and gradually increases showing peak values at frequencies 10.5 and 20.1 Hz. This observation suggests that resonance response starts beyond 6 Hz with the fundamental resonance frequency located at 10.5 Hz. Similar results were obtained for the X-direction (Figure 17a-b), with peak resonance located at 12.3 Hz. It is worth noting that the fundamental period of the tower is expected around 3–4 Hz. Hence, it is possible

that the field experiments cannot measure the fundamental frequency by using the current system at the end of construction because the reliable frequencies were greater than 3 Hz in Figure 17. If the noises are dominant around these frequencies, it is required to increase the amplitude of the signals by increasing the concrete weight or dropping height.

Figure 18 shows the comparison of the observed natural frequencies with those recorded on historical masonry towers (Testa, Barontini, and Lourenço 2023). Although the data lie outside the range of available heights in the literature, they follow reasonably well the general trend which suggests that the field experiments characterize realistically the natural vibration frequencies of Hindu Mandir.

For consistency with the construction stage at the time of the field testing, an additional FE model was developed up to the first-floor level of the structure
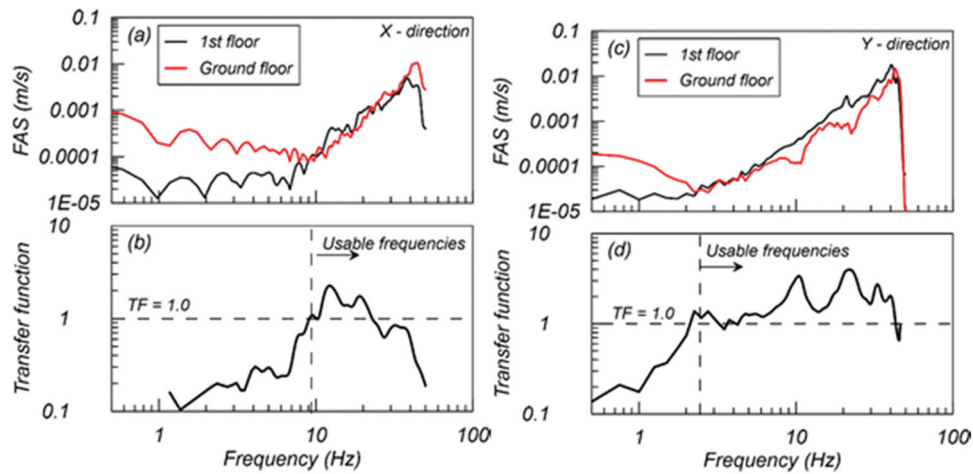
Figure 17. Averaged Fourier amplitude spectra in (a) X-, (c) Y-directions at ground and first-floor levels; averaged transfer functions in (b) X-, (d) Y-directions at ground to first-floor levels.
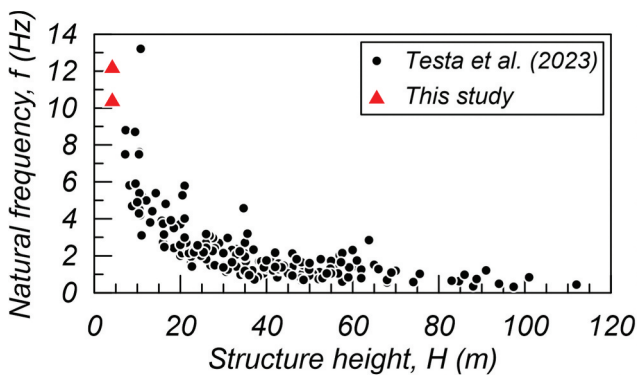
Figure 18. Comparison of the observed natural frequencies at Hindu Mandir with those by historical masonry towers.

Figures 20c-d show a clear peak at 10 *Hz* for Y-direction, without higher-mode resonances. Similar trends were obtained for X-direction (Figure 20a-b). Table 5 provides the comparison in the resonance frequencies of X- and Y- directions between field observations and numerical analyses. The values are relatively consistent for both directions even though the field measurements show slightly higher values than the numerical ones. This observation validates that the structural elements were reasonably modelled such as concrete foundation with sandboxes, slabs and walls made of natural stones and bricks to evaluate the structural dynamic responses.

4. Optimal sensor placement

Optimal sensor placements were determined for SHM using the validated FE models. Modal response analyses were conducted with the local model (Figure 8)

(Figure 19). Time series analyses were conducted to determine the response at the ground and first floor levels at this construction stage. The resulting FAS and TFs in X- and Y-directions are plotted in Figure 20.
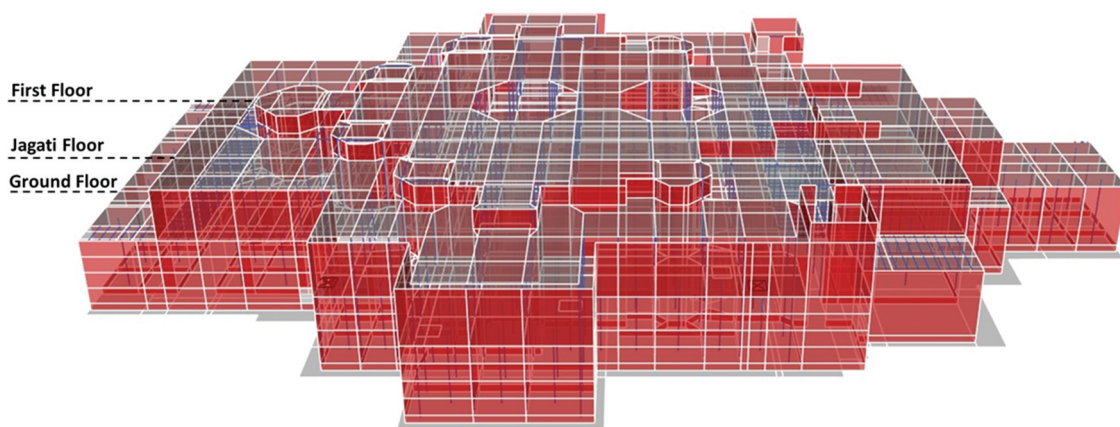
Figure 19. A model from foundation to first-floor level representing construction stage at the time of field testing.
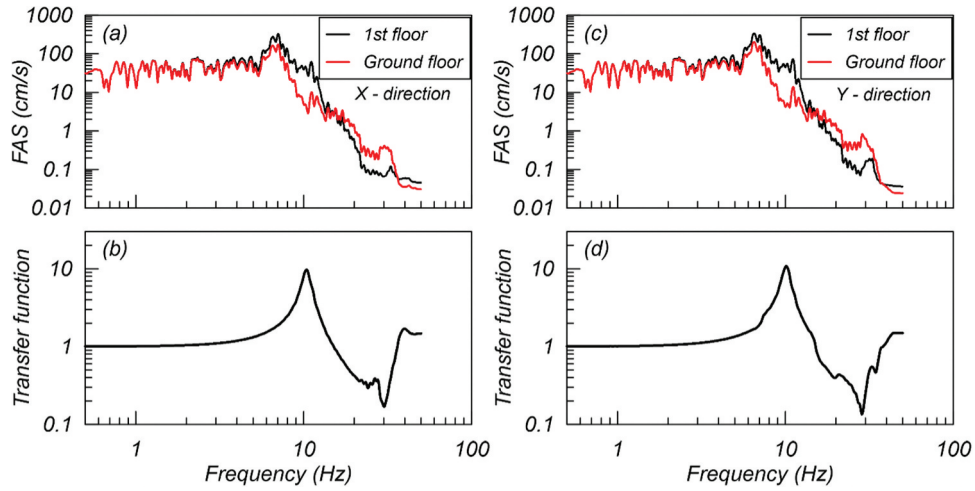
Figure 20. Numerically obtained Fourier amplitude spectra in (a) X-, (c) Y-directions; transfer functions in (b) X-, (d) Y-direction at first and ground floors.

Table 5. Comparison of the observed fundamental and numerically calculated resonance frequencies.

Direction	Numerical Simulation	Field Test
X	10.4	12.3
Y	10.1	10.5

for two horizontal directions using spectral-matched ground motions following ADIBC. There are 221 nodes in the local FE model. Maximum displacements for each node were obtained using the first 16 eigenmodes to obtain a mass participation ratio greater than 90%. Figure 8 and Table 6 illustrate 13 important nodes from the local model by computing DIs using Equations (5) and (6) (Moussas and Pnevmatikos 2019). Two nodes were selected from each floor level with the descending order of DI.

$$DI_N = \sum_{j=1}^{m} DI_{Nj} \qquad (5)$$

where

$$DI_{Nj} = \sqrt{\sum_{i=1}^{3} \left(M_N \times u_{Nj,i} \right)^2} \qquad (6)$$

DI_N is the displacement index at node N. j represents the jth mode, where m is the number of the significant modes. m of 16 was selected in this study to cover a mass participation ratio greater than 90%. i is the displacement component in X, Y, Z directions. M_N is the mass assigned to node N. $u_{Nj,i}$ represents the jth-mode displacement at node N in i direction. The M_N and $u_{Nj,i}$ can be extracted after the analysis. The most important nodes are, in descending order: 1, 2, 3 and 4 (Figure 8). The nodes at the same floor level show the similar DI, where the acceleration time series are strongly correlated between these. These results were obtained because the DI does not consider the spatial correlations between different sensor locations. A similar discussion about how to avoid redundant data is available in (Chang and Pakzad 2014; Vuran, Akan, and Akyildiz 2004).

Table 6. Important sensor locations based on DI and total variance reduction.

	Importance by DI		Importance by total variance reduction	
Order No.	Node No.	Floor	Node No.	Floor
1	1	Flag Point 1	4	Terrace Floor
2	2	Flag Point 2,3	10	First Floor
3	3	Flag Point 2,3	6	Flag Point 6,7
4	4	Terrace Floor	12	Shikhar 1 Beam
5	5	Terrace Floor	2	Flag Point 2,3
6	6	Flag Point 6,7	8	Raised Ceiling
7	7	Flag Point 6,7	1	Flag Point 1
8	8	Raised Ceiling	7	Flag Point 6,7
9	9	Raised Ceiling	11	First Floor
10	10	First Floor	5	Terrace Floor
11	11	First Floor	3	Flag Point 2,3
12	12	Shikhar 1 Beam	13	Shikhar 1 Beam
13	13	Shikhar 1 Beam	9	Raised Ceiling

This study has revised the DI methodology for selecting optimal sensor locations by considering spatial correlation. The selected $n = 13$ important locations were ordered based on the reduction of the total variance conditioned on the selected sensor location. This approach requires the correlation and covariance matrix of the recorded signals. In past studies, the spatial correlation was modelled with the Gaussian function (Chang and Pakzad 2014). In this model, the spatial correlation is 1 if the separated distance between two nodes equals 0 and decreases exponentially as the distance increases. However, as far as we understand, there is no study on the correlation of recorded accelerations for seismic structural response. Therefore, the spatial correlation model cannot be applied to the analyses. To overcome the problem, this study used time series analyses results by the FM model to develop the covariance matrix. The covariance matrix was computed from the PSA at n important nodes. The PSA was selected in this study because it represents the variation of frequency contents of the recorded signals (Hudson 1979). Equations (7) and (8) were employed to compute the covariance matrix (Johnson and Wichern 2007).

$$s_{kk} = \frac{1}{N}\sum_{j=1}^{N}\left(x_{jk} - \bar{x}_k\right)^2, \qquad (7)$$

$$s_{ik} = \frac{1}{N}\sum_{j=1}^{N}\left(x_{ji} - \bar{x}_i\right)\left(x_{jk} - \bar{x}_k\right) \qquad (8)$$

where s_{kk} is the variance, s_{ik} is the covariance of i and k locations, x_{jk} is the PSA value at period j and location k, $\bar{x}_k$ is the mean PSA value at location k, and N is the number of measurements. Since PSA was computed for 108 different natural periods, from .01 s to 10 s for two directions, $N = 216$ in this case because two horizontal directions are considered. By using the above equations, the covariance matrix was obtained from dynamic analyses. The correlation coefficients (Johnson and Wichern 2007) were calculated as:

$$r_{ik} = \frac{s_{ik}}{\sqrt{s_{ii}}\sqrt{s_{kk}}}. \qquad (9)$$

Figure 21 shows the flowchart for placing in order of importance the n selected locations by using the correlation and covariance of the recorded signals. m is the entire number of nodes. j represents the jth important node, where i is the loop to find the jth important node from $(m - j + 1)$ nodes. The highly correlated locations (e.g., $r > .99$) were eliminated randomly to avoid the singularity of the inverse matrix (Figure 21). The conditional sensor locations were ranged to find the
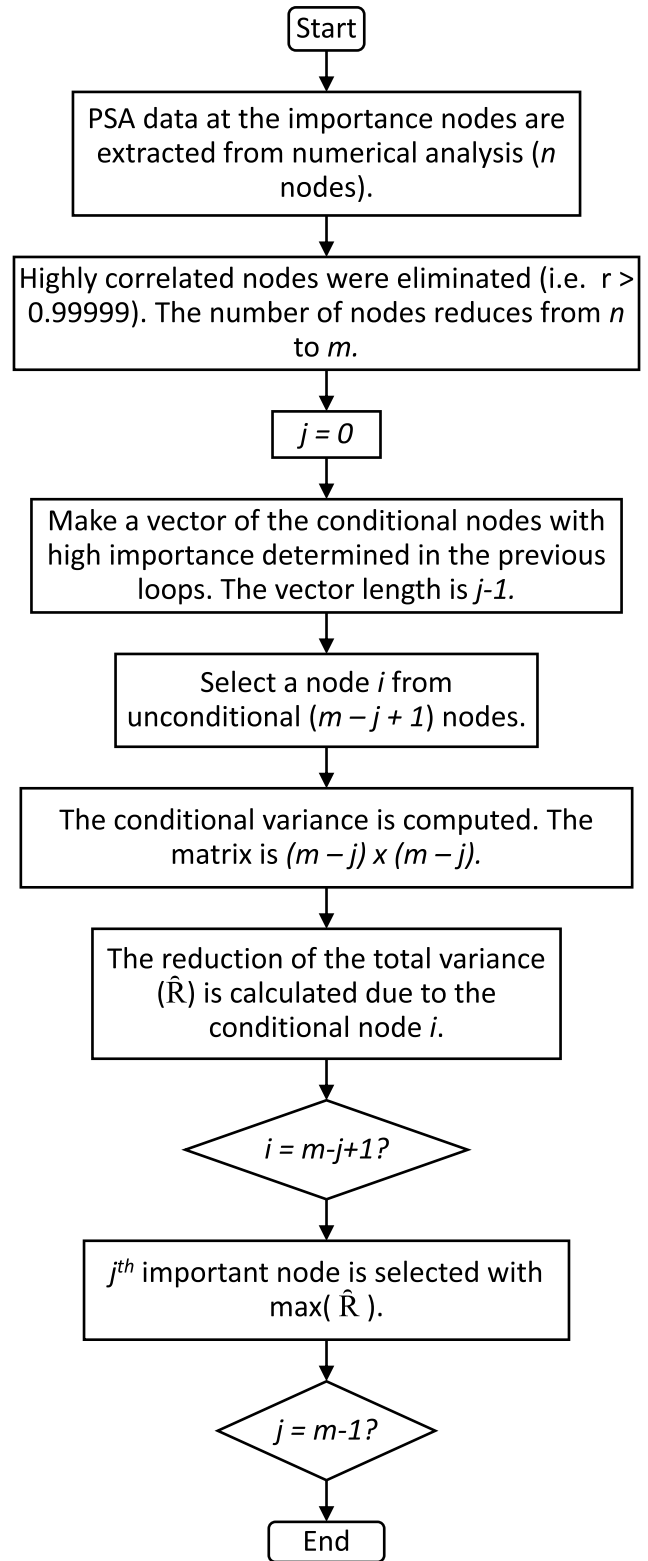

Figure 21. Flowchart of the proposed methodology for selecting optimal sensor locations based on the total variance reduction.

maximum reduction of the variance. The locations with the largest variance reduction due to conditional measurements were selected for the optimal sensor

placement, by which the impacts of the correlations with other locations were evaluated. The following equations show the conditional variance and reduction of the total variance, respectively.

$$\Sigma_{Y_1|Y_2} = \Sigma_{11} - \Sigma_{12}\Sigma_{22}^{-1}\ _{21}, \qquad (10)$$

$$\hat{R} = 1 - \frac{\mathrm{tr}\left(\Sigma_{Y_1|Y_2}\right)}{\mathrm{tr}(\Sigma)} \qquad (11)$$

where $\sum_{22}$ and $\sum_{11}$ are covariance matrices within selected locations and within unselected locations. $\sum_{12}$ is the covariance matrix between selected and unselected locations. Table 6 shows the resulting order of the important nodes by following this approach. The most important node is 4 in Figure 8, following by 10, 6, and 12. The important sensor locations tend to be selected from different floor levels because the influence of the nodes decreases in Equation (11) if the sensor is placed into highly correlated locations. The approach presented in Figure 21 is practical and effective, and it has not been employed in the past. Further improvement is expected by developing the spatial correlation models using the actual observations instead of simulated data because it includes the environmental and sensor noises in the covariance matrix.

5. Conclusions

This study investigates the optimal accelerometer placements for SHM of a complex unreinforced stone masonry structure (Hindu Mandir) in Abu Dhabi. The SHM is required based on the guidelines of Abu Dhabi government, because the building code does not cover unreinforced stone masonry structures like the one at hand. The study illustrates a practical four-step approach for selecting the accelerometer locations. The first step is the identification of potential damage locations based on dynamic analyses. To this end, a "global" structural model of the entire Mandir was developed using FEM, and verified by field experiments during the construction phases. The Main Shikhar tower was identified as the potentially most vulnerable location based on the calculated values of resonance periods and peak displacements. In the second step, a "local" model was developed for the Main Shikhar by placing springs at the structure-to-structure boundaries. Lateral point loads were applied to obtain the linear-elastic spring stiffness matrix at the model boundaries after removing Main Shikhar from the stiffness matrix. The inertial and viscous forces are negligible at the interface model between the local and the rest of the structure, while pseudo-static behavior was considered as an approximation for the rest of the structure. The results show that the natural periods and the eigenmodes for global and local models are sufficiently similar, indicating that the Main Shikhar is sufficiently separated by the local model. This approach is practical but has not been employed in the past, based on our literature review, to develop local models for massive stone masonry structures. In the third step, modal response analyses were conducted using the developed local model to evaluate the response to seismic loads. Thirteen important nodes were selected by considering 16 eigenmodes to cover 90% of mass participation. Had the global model been analyzed directly (without using a local model), this process would require substantial computation time and development of algorithms (*e.g.* Gomes et al. 2019; Guo et al. 2004). In the fourth and last step, the PSA obtained from the time series analyses of the local model was used to develop the covariance matrix by considering the correlations between different accelerometers. Based on the reduction of total variance due to the installation of the accelerometers with conditional probability theory, the optimal locations were selected. This approach is novel and practical for sensor installations to measure less-correlated acceleration signals, and avoids employing redundant acceleration measurements. Through the proposed steps, the locations of the accelerometers can be practically/realistically selected for SHM of massive and complex structures such as the unreinforced stone masonry Hindu Mandir in Abu Dhabi.

Disclosure statement

No potential conflict of interest was reported by the author(s).

References

Abdullah, M. M., A. Richardson, and J. Hanif. 2001. Placement of sensors/actuators on civil structures using genetic algorithms. *Earthquake Engineering and Structural Dynamics* 30 (8):1167–84. doi:10.1002/eqe.57.

Aktan, A. E., and J. M. W. Brownjohn. 2013. Structural Identification: Opportunities and Challenges. *Journal of Structural Engineering* 139 (10):1639–47. doi:10.1061/(asce)st.1943-541x.0000723.

Allemang, R. J. 2003. The modal assurance criterion - twenty years of use and abuse. *Sound and Vibration* 37 (8):14–21.

Altunışık, A. C., F. Y. Okur, and V. Kahya. 2017. Modal parameter identification and vibration based damage detection of a multiple cracked cantilever beam. *Engineering Failure Analysis* 79 (April):154–70. doi:10.1016/j.engfailanal.2017.04.026.

Argyris, C., C. Papadimitriou, and P. Panetsos. 2017. Bayesian optimal sensor placement for modal identification of civil infrastructures. *Journal of Smart Cities* 2 (2):69–86. doi:10.18063/jsc.2016.02.001.

Barsocchi, P., Bartoli, G., Betti, M., Girardi, M., Mammolito, S., Pellegrini, D. and Zini, G. 2021. Wireless sensor networks for continuous structural health monitoring of historic Masonry towers. *International Journal of Architectural Heritage* 15 (1):22–44. doi:10.1080/15583058.2020.1719229.

Basto, C., L. Pelà, and R. Chacón. 2017. Open-source digital technologies for low-cost monitoring of historical constructions. *Journal of Cultural Heritage* 25:31–40. doi:10.1016/j.culher.2016.12.003.

Behnia, A., Chai, H.K., Yorikawa, M., Momoki, S., Terazawa, M. and Shiotani, T. 2014. Integrated non-destructive assessment of concrete structures under flexure by acoustic emission and travel time tomography. *Construction and Building Materials* 67 (PART B):202–15. doi:10.1016/j.conbuildmat.2014.05.011.

Bianconi, F., G. P. Salachoris, F. Clementi, and S. Lenci. 2020 Jun 10. A genetic algorithm procedure for the automatic updating of FEM based on ambient vibration tests. *Sensors (Basel)* 20 (11) : 3315. 10.3390/s20113315.

Borcherdt, R. D., and J. F. Gibbs. 1976. Effects of local geological conditions in the San Francisco Bay region on ground motions and the intensities of the 1906 earthquake. *Bulletin of the Seismological Society of America* 66 (2):467–500. doi:10.1785/BSSA0660020467.

Carne, T. G., and C. R. Dohrmann. 1994. *A modal test design strategy for model correlation*. Albuquerque, NM (United States): Sandia National Labs.

Casapulla, C., L. U. Argiento, and A. Maione. 2018. Seismic safety assessment of a masonry building according to Italian guidelines on cultural heritage: Simplified mechanical-based approach and pushover analysis. *Bulletin of Earthquake Engineering* 16 (7):2809–37. doi:10.1007/s10518-017-0281-9.

Castellazzi, G., A. M. D'Altri, S. de Miranda, and F. Ubertini. 2017. An innovative numerical modeling strategy for the structural analysis of historical monumental buildings. *Engineering Structures* 132:229–48. doi:10.1016/j.engstruct.2016.11.032.

Çatbaş, F. N., T. Kijewski-Correa, and A. E. Aktan. 2013. Structural identification of constructed systems: Approaches, methods, and technologies for effective practice of st-id, structural identification of constructed systems: Approaches, methods, and technologies for effective practice of st-id. doi:10.1061/9780784411971.

Cawley, P. 2018. Structural health monitoring: Closing the gap between research and industrial deployment. *Structural Health Monitoring* 17 (5):1225–44. doi:10.1177/1475921717750047.

Ceravolo, R., G. Pistone, L. Z. Fragonara, S. Massetto, and G. Abbiati. 2016. Vibration-based monitoring and diagnosis of cultural heritage: A methodological discussion in three examples. *International Journal of Architectural Heritage* 10 (4):375–95. doi:10.1080/15583058.2013.850554.

Chamberlain, C. J., C. J. Hopp, C. M. Boese, E. Warren-Smith, D. Chambers, S. X. Chu, K. Michailos, and J. Townend. 2018. Eqcorrscan: Repeating and near-repeating earthquake detection and analysis in python. *Seismological Research Letters* 89 (1):173–81. doi:10.1785/0220170151.

Chang, M., and S. N. Pakzad. 2014. Optimal sensor placement for modal identification of bridge systems considering number of sensing nodes. *Journal of Bridge Engineering* 19 (6):1–10. doi:10.1061/(asce)be.1943-5592.0000594.

Chiu, P., and F. Y. Lin. 2004. A simulated annealing algorithm to support the sensor placement for target location. Canadian conference on electrical and computer engineering 2004 vol. 2, Niagara Falls, ON, Canada, Piscataway, NJ: IEEE, 2–5 May 2004, pp. 867–70.

Cigada, A., L. Corradi Dell'acqua, B. Mörlin Visconti Castiglione, M. Scaccabarozzi, M. Vanali, and E. Zappa. 2017. Structural health monitoring of an historical building: The main spire of the Duomo Di Milano. *International Journal of Architectural Heritage* 11 (4):501–18. doi:10.1080/15583058.2016.1263691.

CSI. 2018. *ETABS v17 Integrated Analysis, design and drafting of building systems*. Berkely, CA, USA: Computers and Structures Inc.

D'Ayala, D., and S. Lagomarsino. 2015. Performance-based assessment of cultural heritage assets: Outcomes of the European FP7 PERPETUATE project. *Bulletin of Earthquake Engineering* 13 (1):5–12. doi:10.1007/s10518-014-9710-1.

DMA. 2013. *Abu dhabi international building code*. (ADIBC), Abu Dhabi Department of Municipal Affairs.

Farrar, C. R., and K. Worden. 2007. An introduction to structural health monitoring. *Philosophical Transactions of the Royal Society A: Mathematical, Physical and Engineering Sciences* 365 (1851):303–15. doi:10.1098/rsta.2006.1928.

García-Macías, E., and F. Ubertini. 2022. Least angle regression for early-stage identification of earthquake-induced damage in a monumental masonry palace: Palazzo dei Consoli. *Engineering Structures* 259 (August 2021):114119. doi:10.1016/j.engstruct.2022.114119.

Gomes, G. F., F. A. de Almeida, P. da Silva Lopes Alexandrino, S. S. da Cunha, B. S. de Sousa, and A. C. Ancelotti. 2019. A multiobjective sensor placement optimization for SHM systems considering Fisher information matrix and mode shape interpolation. *Engineering with Computers* 35 (2):519–35. doi:10.1007/s00366-018-0613-7.

Guo, H. Y., L. Zhang, L. L. Zhang, and J. X. Zhou. 2004. Optimal placement of sensors for structural health

monitoring using improved genetic algorithms. *Smart Materials and Structures* 13 (3):528–34. doi:10.1088/0964-1726/13/3/011.

Hassani, S., and U. Dackermann. 2023. A systematic review of optimization algorithms for structural health monitoring and optimal sensor placement. *Sensors* 23 (6). doi: 10.3390/s23063293.

He, R. S., and S. F. Hwang. 2006. Damage detection by an adaptive real-parameter simulated annealing genetic algorithm. *Computers & Structures* 84 (31–32):2231–43. doi:10.1016/j.compstruc.2006.08.031.

Herráiz, D. R., Soga, K., Fidler, P., De Battista, N. (2016) Wireless sensor networks for civil infrastructure monitoring: A best practice guide. ISBN=9780727761514.

Housner, G. W., L. A. Bergman, T. K. Caughey, A. G. Chassiakos, R. O. Claus, S. F. Masri, R. E. Skelton, T. T. Soong, B. F. Spencer, and J. T. P. Yao. 1997. Structural Control: Past, Present, and Future. *Journal of Engineering Mechanics* 123 (9):897–971. doi:10.1061/(asce)0733-9399 (1997)123:9(897). Available at

Hudson, D. E. 1979. Reading and interpreting strong motion accelerograms. In *Engineering monographs on earthquake criteria, structural design, and strong motion records*, Vol 1, 112. Berkeley, CA: Earthquake Engineering Research Institute.

ICC. 2018. International building code 2018, 6th Version November 2021, ICC Digital Codes. https://codes.iccsafe.org/content/IBC2018P6/index

IS 1905. 1987. *Code of practice for structural use of unreinforced masonry (third revision), bureau of Indian standards (BIS), civil engineering, building construction practices including painting*. Varnishing and Allied Finishing (CED 13).

Jassim, Z. A., N. N. Ali, F. Mustapha, and N. A. Abdul Jalil. 2013. A review on the vibration analysis for a damage occurrence of a cantilever beam. *Engineering Failure Analysis* 31:442–61. doi:10.1016/j.engfailanal.2013.02.016.

Johnson, R. A., and D. W. Wichern. 2007. *Applied Multivariate Statistical Analysis*. 6th ed., 671–757. Prentice Hall: Pearson.

Kim, S., Pakzad, S., Culler, D., Demmel, J., Fenves, G., Glaser, S. and Turon, M. 2007. Health monitoring of civil infrastructures using wireless sensor networks. *iPSN 2007: Proceedings of the Sixth International Symposium on Information Processing in Sensor Networks*:254–63. doi:10.1145/1236360.1236395.

Kishida, T., D.-S. Park, R. Sousa, R. Armstrong, and Y.-J. Byon. 2020. Modulus reduction of embankment dams based on downhole array time series. *Earthquake Spectra* 36 (1):400–21. doi:10.1177/8755293019878182.

Koh, C. G., B. Hong, and C. Y. Liaw. 2003. Substructural and progressive structural identification methods. *Engineering Structures* 25 (12):1551–63. doi:10.1016/S0141-0296(03)00122-6.

Konno, K., and T. Ohmachi. 1998. Ground-motion characteristics estimated from spectral ratio between horizontal and vertical components of microtremor. *Bulletin of the Seismological Society of America* 88 (1):228–41. doi:10.1785/bssa0880010228.

Krischer, L., T. Megies, R. Barsch, M. Beyreuther, T. Lecocq, C. Caudron, and J. Wassermann. 2015. ObsPy: A bridge for seismology into the scientific python ecosystem. *Computational Science and Discovery* 8 (1):014003. doi:10.1088/1749-4699/8/1/014003.

Ktenidou, O. J., F.-J. Chávez-García, D. Raptakis, and K. D. Pitilakis. 2016. Directional dependence of site effects observed near a basin edge at Aegion, Greece. *Bulletin of Earthquake Engineering* 14 (3):623–45. doi:10.1007/s10518-015-9843-x.

Lacanna, G., M. Ripepe, M. Coli, R. Genco, and E. Marchetti. 2019. Full structural dynamic response from ambient vibration of Giotto's bell tower in firenze (Italy), using modal analysis and seismic interferometry. *NDT & E International* 102 (November):9–15. doi:10.1016/j.ndteint.2018.11.002.

Lagomarsino, S., and S. Cattari. 2015. PERPETUATE guidelines for seismic performance-based assessment of cultural heritage masonry structures. *Bulletin of Earthquake Engineering* 13 (1):13–47. doi:10.1007/s10518-014-9674-1.

LeBrun, B., D. Hatzfeld, and P. Bard. 2001. Site Effect Study in Urban Area: Experimental Results in Grenoble (France). *Geofisica Pura e Applicata* 158 (12):2543–57. doi:10.1007/PL00001185.

Li, B., A. Der Kiureghian, and S. K. Au. 2018. A Gibbs sampling algorithm for structural modal identification under seismic excitation. *Earthquake Engineering and Structural Dynamics* 47 (14):2735–55. doi:10.1002/eqe.3094.

Li, J., X. Zhang, J. Xing, P. Wang, Q. Yang, and C. He. 2015. Optimal sensor placement for long-span cable-stayed bridge using a novel particle swarm optimization algorithm. *Journal of Civil Structural Health Monitoring* 5 (5):677–85. doi:10.1007/s13349-015-0145-4.

Ludeno, G., N. Cavalagli, F. Ubertini, F. Soldovieri, and I. Catapano. 2020. On the combined use of ground penetrating radar and crack meter sensors for structural monitoring: Application to the Historical Consoli Palace in Gubbio, Italy. *Surveys in Geophysics* 41 (3):647–67. doi:10.1007/s10712-019-09526-y.

Megies, T., M. Beyreuther, R. Barsch, L. Krischer, and J. Wassermann. 2011. ObsPy – what can it do for data centers and observatories? *Annals of Geophysics* 54 (1):47–58. doi:10.4401/ag-4838.

Meyer, P., J. Ochsendorf, J. Germaine, and E. Kausel. 2007. The impact of high-Frequency/Low-energy seismic waves on unreinforced masonry. *Earthquake Spectra* 23 (1):77–94. doi:10.1193/1.2431211.

Monchetti, S., C. Viscardi, M. Betti, and F. Clementi. 2023. Comparison between Bayesian updating and approximate Bayesian computation for model identification of masonry towers through dynamic data. *Bulletin of Earthquake Engineering*. doi:10.1007/s10518-023-01670-6.

Moussas, V. C., and N. Pnevmatikos. 2019. Sensor placement selection for SHM of buildings. *COMPDYN Proceedings* 2:2186–95. doi:10.7712/120119.7069.19633.

Muin, S., and K. M. Mosalam. 2017. Cumulative absolute velocity as a local damage indicator of instrumented structures. *Earthquake Spectra* 33 (2):641–64. doi:10.1193/090416EQS142M.

Nanometrics inc. 2015. *Trillium posthole user Guide*. Canada: Nanometrics Inc.

Ng, C. T. 2014. Application of Bayesian-designed artificial neural networks in phase ii structural health monitoring

benchmark studies. *Australian Journal of Structural Engineering* 15 (1):27–36. doi:10.7158/S12-042.2014.15.1.

Oreta, A. W. C., and T. Tanabe. 1993. Localized identification of structures by Kalman filger. *Structural Engineering/Earthquake Engineering* 9 (4):217s–25s.

Pandey, A., M. Biswas, and M. Samman. 1991. Damage detection from changes in curvature mode shapes. *Journal of Sound and Vibration* 145 (2):321–32. doi:10.1016/0022-460X(91)90595-B.

Pardalopoulos, S. I., and S. J. Pantazopoulou. 2017. Methodology for practical seismic assessment of unreinforced masonry buildings with historical value. *Earthquake Engineering and Structural Dynamics* 46 (15):2793–810. doi:10.1002/eqe.2931.

Park, D. S., and T. Kishida. 2019. Seismic response of embankment dams based on recorded strong-motion data in Japan. *Earthquake Spectra* 35 (2):955–76. doi:10.1193/042918EQS107M.

Park, C. B., R. D. Miller, and J. Xia. 1999. Multichannel analysis of surface waves. *Geophysics* 64 (3):800–08. doi:10.1190/1.1444590.

Pastor, M., M. Binda, and T. Harčarik. 2012. Modal assurance criterion. *Procedia Engineering* 48:543–48. doi:10.1016/j.proeng.2012.09.551.

Pregnolato, M., S. Gunner, E. Voyagaki, R. De Risi, N. Carhart, G. Gavriel, P. Tully, T. Tryfonas, J. Macdonald, C. Taylor, et al. 2022. Towards civil engineering 4.0: Concept, workflow and application of digital twins for existing infrastructure. *Automation in Construction* 141 (June):104421. doi:10.1016/j.autcon.2022.104421.

Rytter, A. 1993. *Vibrational based inspection of civil engineering structures*. Aalborg University: Dept. of Building Technology and Structural Engineering.

Salachoris, G. P., G. Standoli, M. Betti, G. Milani, and F. Clementi. 2023. Evolutionary numerical model for cultural heritage structures via genetic algorithms: a case study in central Italy. *Bulletin of Earthquake Engineering*. doi:10.1007/s10518-023-01615-z.

Silvestri, S., S. Baraccani, D. Foti, S. Ivorra, D. Theodossopoulos, V. Vacca, J. Ochoa Roman, L. Cavallini, E. Mokhtari, R. White, et al. 2021. Shaking table testing of groin vaults made by 3D printers. *Soil Dynamics and Earthquake Engineering* 150:106880. doi:10.1016/j.soildyn.2021.106880.

Sivori, D., S. Cattari, and M. Lepidi. 2022. A methodological framework to relate the earthquake-induced frequency reduction to structural damage in masonry buildings. *Bulletin of Earthquake Engineering* 20 (9):4603–4638. doi:10.1007/s10518-022-01345-8.

Standoli, G., G. P. Salachoris, M. G. Masciotta, and F. Clementi. 2021. Modal-based FE model updating via genetic algorithms: Exploiting artificial intelligence to build realistic numerical models of historical structures. *Construction and Building Materials* 303:124393–618. doi:10.1016/j.conbuildmat.2021.124393.

Sun, Z., and C. C. Chang. 2004. Statistical wavelet-based method for structural health monitoring. *Journal of Structural Engineering* 130 (7):1055–62. doi:10.1061/(asce)0733-9445(2004)130:7(1055).

Tan, Y., and L. Zhang. 2020. Computational methodologies for optimal sensor placement in structural health monitoring: A review. *Structural Health Monitoring* 19 (4):1287–308. doi:10.1177/1475921719877579.

Tena-Colunga, A. 1992. Seismic evaluation of unreinforced masonry structures with flexible diaphragms. *Earthquake Spectra* 8 (2):305–18. doi:10.1193/1.1585683.

Testa, F., A. Barontini, and P. B. Lourenço. 2023. Development and validation of empirical formulations for predicting the frequency of historic masonry towers. *International Journal of Architectural Heritage* 1–21. doi:10.1080/15583058.2023.2217127.

Todorovska, M. I., and M. D. Trifunac. 2007. Earthquake damage detection in the imperial county services building I: The data and time–frequency analysis. *Soil Dynamics and Earthquake Engineering* 27 (6):564–76. doi:10.1016/j.soildyn.2006.10.005.

Torelli, G., D'Ayala, D., Betti, M. and Bartoli, G. 2020. Analytical and numerical seismic assessment of heritage masonry towers, bulletin of earthquake engineering. *Springer Netherlands*. doi:10.1007/s10518-019-00732-y.

Vuran, M. C., Ö. B. Akan, and I. F. Akyildiz. 2004. Spatio-temporal correlation: Theory and applications for wireless sensor networks. *Computer Networks* 45 (3):245–59. doi:10.1016/j.comnet.2004.03.007.

Wiercigroch, M. 2018. Mechanical vibrations: Theory and application to Structural Dynamics – 3rd edition M. Geradin and D. J. Rixen John Wiley and sons, the atrium, Southern Gate, Chichester, West Sussex, PO19 8SQ, UK. 2015. 598pp. Illustrated. £83.95. ISBN 978-1-118-90020 8. *Aeronautical Journal* 122 (1251):857–857. doi:10.1017/aer.2018.27.

Woolery, E., R. Street, and P. Hart. 2009. Evaluation of linear site-response methods for estimating higher-frequency (> 2 hz) ground motions in the lower Wabash River valley of the central United States. *Seismological Research Letters* 80 (3):525–38. doi:10.1785/gssrl.80.3.525.

Yang, Y., M. Chadha, Z. Hu, and M. D. Todd. 2022. An optimal sensor placement design framework for structural health monitoring using Bayes risk. *Mechanical Systems and Signal Processing* 168 (108618):ISSN 0888–3270. doi:10.1016/j.ymssp.2021.108618.

Yao, L., W. A. Sethares, and D. C. Kammer. 1993. Sensor placement for on-orbit modal identification via a genetic algorithm. *AIAA Journal* 31 (10):1922–28. doi:10.2514/3.11868.

Yi, T., H. Li, and M. Gu. 2011a. A new method for optimal selection of sensor location on a high-rise building using simplified finite element model. *Structural Engineering and Mechanics* 37 (6):671–84. doi:10.12989/sem.2011.37.6.671.

Yi, T., H. Li, and M. Gu. 2011b. Optimal Sensor Placement for Health Monitoring of High-Rise structure based on genetic algorithm 2011. *Mathematical Problems in Engineering* 395101:1–12. doi:10.1155/2011/395101.

Zhu, C., F. Cotton, and M. Pilz. 2020. Detecting site resonant frequency using HVSR: Fourier versus response spectrum and the first versus the highest peak frequency. *Bulletin of the Seismological Society of America* 110 (2):427–40. doi:10.1785/0120190186.